applied sciences

MDPI

Article

Galerkin Finite Element Process for Entropy Production and Thermal Evaluation of Third-Grade Fluid Flow: A Thermal Case Study

Faisal Shahzad [1], Wasim Jamshed [1,*], El Sayed M. Tag El Din [2], Rabia Safdar [3], Nor Ain Azeany Mohd Nasir [4], Rabha W. Ibrahim [5], Syed M. Hussain [6], Ikram Ullah [7], Muhammad Bilal Hafeez [8] and Marek Krawczuk [8]

[1] Department of Mathematics, Capital University of Science and Technology (CUST), Islamabad 44000, Pakistan
[2] Electrical Engineering, Faculty of Engineering and Technology, Future University in Egypt, New Cairo 11835, Egypt
[3] Department of Mathematics, Lahore College for Women University, Lahore 54000, Pakistan
[4] Department of Mathematics, Centre for Defence Foundation Studies, Universiti Pertahanan Nasional Malaysia, Kem Sungai Besi, Kuala Lumpur 57000, Malaysia
[5] Department of Mathematics, Mathematics Research Center, Near East University, Near East Boulevard, Via Mersin 10, 99138 Nicosia, Turkey
[6] Department of Mathematics, Faculty of Science, Islamic University of Madinah, Medina 42351, Saudi Arabia
[7] Department of Sciences and Humanities, National University of Computer and Emerging Sciences, Peshawar 25000, Pakistan
[8] Institute of Mechanics and Machine Design, Faculty of Mechanical Engineering and Ship Technology, Gdansk University of Technology, Narutowicza 11/12, 80-233 Gdańsk, Poland
* Correspondence: wasiktk@hotmail.com

Citation: Shahzad, F.; Jamshed, W.; Tag El Din, E.S.M.; Safdar, R.; Mohd Nasir, N.A.A.; Ibrahim, R.W.; Hussain, S.M.; Ullah, I.; Hafeez, M.B.; Krawczuk, M. Galerkin Finite Element Process for Entropy Production and Thermal Evaluation of Third-Grade Fluid Flow: A Thermal Case Study. *Appl. Sci.* **2022**, *12*, 9647. https://doi.org/10.3390/app12199647

Academic Editor: Francesca Scargiali

Received: 4 August 2022
Accepted: 21 September 2022
Published: 26 September 2022

Abstract: A fluid's moving class improves its heat transmission capability, as well as its rigidity, owing to multivariate molecule suspension. In this way, nanofluids are superior to common fluids. In this study, we evaluated the features of ease and heat transfer. Furthermore, we investigated permeable media, heat source, variable heat conductivity, and warm irradiation results. A mathematical technique known as the Galerkin finite element (G-FEM) approach was used to solve the supervising conditions. Third-grade nanofluid (TGNF), which consists of two types of nanoparticles (NPs), single-walled carbon nanotubes (SWCNT), and multi-walled carbon nanotubes (MWCNTs) distributed in a base liquid of carboxymethyl cellulose (CMC) water, was used for this examination. The main conclusion of this study is that MWCNT-CMC nanofluid has a higher heat transfer velocity than SWCNT-CMC nanofluid. The entropy of the framework can be increased by adjusting the thermal conductivity. Additionally, we found that increasing the main volume section decreases the speed but increases the dispersion of atomic energy. In order to separately account for the development properties of inertial forces and shallow heat dispersion forces, Reynolds and Brinkman values can be used to accelerate the entropy rate of the heating framework.

Keywords: third-grade nanofluid; carbon nanotubes; variable thermal conductivity; entropy generation; Galerkin finite element method

1. Introduction

Heat transfer (HT) is a branch of thermal engineering that integrates the production, use, conversion, and exchange of thermodynamic across movable systems. Thermal conduction, current convection, thermal radiation, and dynamic assignment via phase shifts are all HT mechanisms. Engineers investigate the transfer of a wide variety of chemical substances (advection mass transfer), either cold or hot, in order to achieve HT. Whereas these strategies have distinct properties, they frequently coexist in the same system. Heat

exchange occurs when a high volume of liquid (gas or liquid) flows through another liquid, transferring heat. All convective processes provide heat for circulation [1]. HT is a critical manufacturing process. Heat must be involved, reduced, or uninvolved from the distribution of one cycle to the next throughout the industrial sector. In theory, the heat lost by a hot liquid is not equal to the temperature gained by a cool liquid due to natural heat loss [2]. In 99 percent of industrial production applications, a specific technique for HT is employed. Drying procedures are all variations on the theme of HT. Industrial applications of HT fluids range from basic, dry designs to sophisticated systems that perform a variety of roles during the manufacturing process. Due to the numerous differences in the design and implementation of HT liquid processes, the number of businesses that employ this technique is likewise considerable [3]. Miniaturization significantly influences heat exchanger technology, making them more compact and efficient. The efficiency of heat exchangers exerts a significant influence on the overall efficiency and health of thermal energy systems. Microchannel heat sinks are a relatively new development in heat exchange technology. The high cohesion of a wide HT surface with a multichannel heat sink makes it an effective heat exchanger for electronic cooling [4].

Nanofluids are liquids that contain nanometer-sized particles, or nanoparticles. Nanoparticles are suspended in the primary liquid in these colloidal fluid suspensions. Metals, oxides, carbides, and carbon nanotubes are the most common nanoparticles employed in nanofluids. Heat has been transferred in many processes using a variety of common fluids. Owing to its low thermal conductivity, water is frequently utilized as a liquid active medium, although it is not considered an efficient medium for heat transfer. There are a number of uses for non-exchange fluids, including motor oil and ethylene glycol, among others. However, their high viscosity and hazardous environments limit their application in HT procedures [5]. Nanoparticles are commonly added to ethylene glycol and water for application as a railway carriage coolant, improving engine cooling performance. Recently, high-performance processors with a maximum power density of 100–300 w/cm^2 have been increasingly used in electronic cooling of integrated and microprocessor circuits [6]. The natural convection HT of Newtonian nanofluid on the outer surface of laminar boundaries has been thoroughly scrutinized. Natural convection HT has been reported to be sensitive to the viscosity model employed and to be defined by more than just the thermal conductivity of the active nanofluid [7]. Since the turn of the century, liquid heat transfer equipment has been supported by estimating possible layers. One of the primary responsibilities of secondary theory is to evaluate the effects of pulling bodies on the current, for example, by dragging a flat plate in an initial position [8]. When injected without incorporation, non-Newtonian nanofluid can achieve superior heat transfer performance to that of Newtonian nanofluid. Although the fundamentals of nanoparticles can be altered during maintenance, such alterations could affect the heat transfer procedure [9].

One of the several subtypes of non-Newtonian liquids discovered by Rivlin and Ericksen [10] is third-grade fluids. Using a three-layered coordinate framework, Hayat et al. [11] examined third-grade fluid with respect to Soret and Dufour effects. Mustafa [12] investigated a variety of stretching plates. Shehzad et al. [13] studied the effects of viscous dispersion and Newtonian warming on nanofluid streams of third-grade fluids. As a part of their investigation of permeable level plates, Sajid et al. [14] employed the limited component approach with a third-grade fluid stream, obtaining a time-subordinated crushing stream between two equal plates. Rashidi et al. [15] analyzed the approximate analytical solution for the unsteady axisymmetric two-dimensional squeezing flows considering parallel plates. Shehzad et al. recently investigated third-grade surface fluid streams [16]. Hussnain et al. [17] studied second-grade fluids in a three-layered turning system. Serdar Baris [18] studied second-grade fluid using a sliding level plate. Shoaib et al. [19] studied second-grade fluids in a limitless flat plane divider with verbose attractions in three dimensions. Second-grade nanofluids with radioactive repercussions across an increasing area were the focus of research by Ramzan et al. [20]. Mustafa et al. [21] examined the

hydromagnetic second grade nanofluid boundary layer flow through a stretched surface assuming the convective boundary conditions. Gyrotactic microorganisms were examined by Alzahrani et al. [22] in a high-level absorbent layer with a third-grade MHD fluid stream. A joule heater is a device that transfers energy across a material, generating heat. Fosdick and Rajagopal studied the thermodynamics and stability of third-grade liquids [23]. After considering liquids in a series, Yurusoy and Pakdemirli [24] settled on third-grade liquids. Ellahi and Riaz [25] used MHD third-grade liquid to assess heat transfer concentration. Adesanya and Makinde [26] examined heat ingestion/age in a third-grade liquid stream [26]. Hayat et al. [27] could not completely rule out using convective pressure to compress a third-grade fluid stream. Akinshilo and Sobamowo [28] observed an appealing third-grade fluid stream. Third-grade liquid was examined with Prandtl sway by Reddy et al. [29]. Over an isothermal cone, Gaffar et al. [30] evaluated a third-grade liquid stream for heat age/ingestion. Sajid et al. theoretically examined a third-grade liquid stream [31]. Using a joule warming effect, Mahanthesh and Joseph [32] determined the evolution of a third-grade fluid. Waqas et al. investigated the production of Jeffrey nanomaterial using gyrotactic bacteria [33]. Recently, Shah et al. [34,35] examined heat-conductive nanofluid streams under the influence of attractive powers through various computations.

The Galerkin finite element method (G-FEM) is a method that partitions the domain into finite elements to compute the numerical solution of differential equations. Piecewise trial functions are used to estimate each element's function. Al-Kouz et al. [36] have solved the Darcy–Brinkman–Forchheimer model for nanofluid (SWCNT-H_2O) flow and HT using G-FEM. The G-FEM was implemented to determine the hydrodynamic and thermal fields in the model. The authors reported that after placing the heating cradle in the lowest enclosure, the convective regime predominated. G-FEM was also used by Hatami and Ghasemi to compute the thermophoresis and Brownian diffusion for two-phase nanofluid flow through a porous vertical cone [37]. G-FEM has been widely used by researchers, for instance, Al-Kouz et al. [38], Khan et al. [39], Abbas et al. [40], Qureshi et al. [41], and Asmadi et al. [42]. Ibrahim and Gadisa [43] reported the numerically calculated values of the local skin friction coefficient and the local Nusselt value correlate with those previously published in the literature. In addition, Mourad et al. calculated a steady MHD hybrid nanofluid using a G-FEM-based numerical solution, achieving comparable accuracy to that previously reported in the literature [44]. For additional details and applications, see refs. [45–49].

Entropy lifetime has recently been studied by researchers with respect to the advancement of liquids and heat across an extended surface. Heating and cooling markers play a vital role in many electrical and energy difficulties. Aiboud and Saouli [50] studied an MHD viscoelastic liquid stream using Kummer's capacity for entropy analysis. Makinde [51] used shooting quadrature to calculate entropy age based on the heat radiation of a semi-boundless plate and the Newtonian warming effects of a variable-consistency liquid. Loganathan et al. [52,53] used a stretchy sheet to examine the entropy of the Williamson and third-grade microliquid streams generated by various impacts. Indirect administration frameworks were addressed with HAM. Structure-unsettling sway is another potential measure of entropy. Thermodynamic systems may have a broad origin, indicating that their values fluctuate depending on the magnitude of the problem, which can be described by the term, "moo entropy". The concept of entropy has quantitative qualities that may be associated with failure or weakness [54]. These concepts can be applied in a range of contexts, from conventional thermodynamics to the principles of information theory, originating in standard thermodynamics but having since gained prominence in mathematical material science. For example, the concept of "moo entropy" has been applied in various scientific and material sciences, including cosmology, economics, sociology, environmental studies, and information technology [55]. From classical thermodynamics, where the concept first emerged, to material knowledge and information theory standards, the terminology and concept have been applied in a variety of contexts.

In the fields of science and material science, cosmology, economic, sociology, environmental science and climate change, and information structures and correspondence-based information transmission [56], this concept has been used in a wide range of applications.

In light of the previously published reports, the objective of this review is to fill a hole by exploring the radiative progression of a third-grade nanofluids (TGNFs), as well as HT with variable temperature and thermal conductivity across an extended surface. The Tiwari and Das nanofluid model was proposed to numerically demonstrate nanofluid streams. SWCNT and MWCNT nanoparticles have been considered, with CMC water used as an establishment fluid. The stream impact can be observed by exploring the entropy age. An appropriate comparability change is utilized to transform governing conditions of the TGNFs into ordinary differential equations (ODEs). Mathematical estimations are used to determine the subsequent ODEs according to the Galerkin finite element method with appropriate parametric boundaries. Graphical designs are used to address mathematical outcomes. Furthermore, we discuss the effect on molecule morphologies, convective slip limit conditions, heat radiation streams, and speed.

2. Mathematical Formulation

A flat, straight, shallow, non-uniform extending velocity is represented by the following mathematical model:

$$\boldsymbol{U_w(x, 0) = bx}. \tag{1}$$

Figure 1 depicts the architecture of the flow model. The sheet is stretched in a single direction, resulting in the displayed form. An additional thermal leap is used to transfer heat from the surface to the fluid during the flow slip occurrence. The sheet is flat and permeable with a stretching velocity of $\boldsymbol{U_w}$ and a temperature of ¥. The solution used for this research contains SWCNT nanoparticles and MWCNT nanoparticles (CMC).

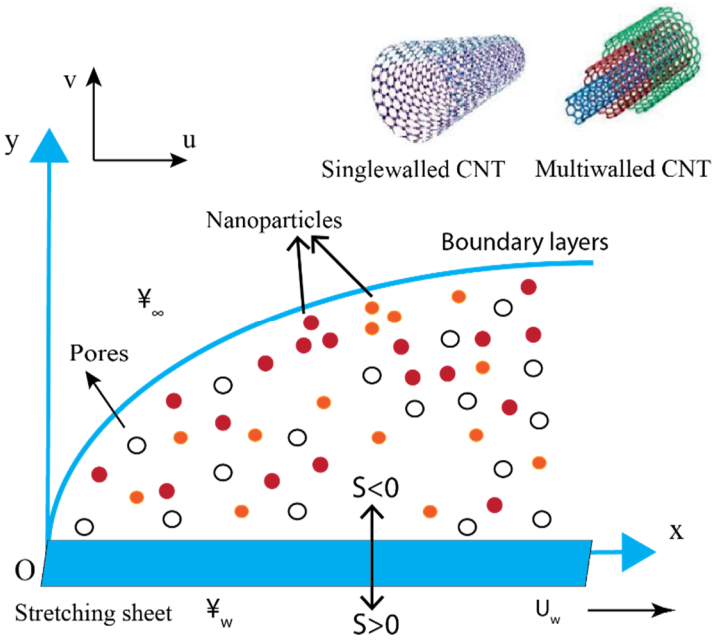

Figure 1. Schematic diagram of the flow model.

2.1. Model Equations

The flow constitutive equations [57] of a severe third-grade nanofluid are included in this study, as follows:

$$\boldsymbol{u_x + u_y = 0}, \tag{2}$$

$$\left.\begin{array}{c} \boldsymbol{uu_x + vu_y = \frac{\mu_{nf}}{\rho_{nf}}\left(u_{yy}\right) + \frac{\lambda_1}{\rho_{nf}}\left(uu_{xyy} + 3u_yu_{xy} + u_xu_{yy} + vu_{yyy}\right) +} \\ \boldsymbol{\frac{2\lambda_2}{\rho_{nf}}\left(u_yu_{xy}\right) + \frac{6\lambda_3}{\rho_{nf}}\left(u_y\right)^2u_{yy} - \frac{\mu_{nf}}{\rho_{nf}}\frac{u}{k},} \end{array}\right\} \quad (3)$$

$$\left.\begin{array}{c} \boldsymbol{u¥_x + v¥_y = \frac{k_{nf}}{(\rho C_p)_{nf}}\left(\frac{\partial}{\partial y}\left(\kappa^*_{nf}(¥)¥_y\right)\right) - \frac{1}{(\rho C_p)_{nf}}\left((q_r)_y\right) + \frac{1}{(\rho C_p)_{nf}}Q(¥ - ¥_\infty)} \\ \boldsymbol{+ \frac{\mu_{nf}}{(\rho C_p)_{nf}}\left(u_y\right)^2.} \end{array}\right\} \quad (4)$$

The relevant boundary conditions are:

$$\left.\begin{array}{c} \boldsymbol{u(x,0) = U_w + N_L\left(u_y\right), v(x,0) = V_w, -k_0\left(¥_y\right) = h_f(¥_w - ¥),} \\ \boldsymbol{u \to 0,\ u_y \to 0, ¥ \to ¥_\infty\ as\ y \to \infty.} \end{array}\right\} \quad (5)$$

The notations $(\boldsymbol{\lambda_1},\ \boldsymbol{\lambda_2},\ \boldsymbol{\lambda_3})$, $\boldsymbol{k}$, $\boldsymbol{Q}$, $\boldsymbol{\kappa^*_{nf}}$, and $\boldsymbol{q_r}$ are the material moduli, permeability of the porous medium, heat-generating parameter, variable thermal conductivity, and radiative heat flux, respectively.

2.2. Thermophysical Features of the Third-Grade Nanofluid

The thermophysical properties of aquatic organisms are improved when nanoparticles are dispersed within them. Table 1 summarizes the third-grade material properties of the investigated nanofluid.

Table 1. The primary properties of the investigated third-grade nanofluid [58].

Property	Nanofluid
Dynamic viscosity	$\mu_{nf} = \mu_f(1-\phi)^{-2.5}$
Density	$\rho_{nf} = (1-\phi)\rho_f + \phi\rho_s$
Heat capacity	$(\rho C_p)_{nf} = (1-\phi)(\rho C_p)_f + \phi(\rho C_p)_s$
Thermal conductivity	$\frac{k_{nf}}{k_f} = \left[\frac{(k_s+2k_f) - 2\phi(k_f-k_s)}{(k_s+2k_f) + \phi(k_f-k_s)}\right]$

Based on Table 1, the parameters $\boldsymbol{\mu_f}$, $\boldsymbol{\rho_f}$, $\boldsymbol{(C_p)_f}$, and $\boldsymbol{\kappa_f}$ are self-motivated viscosity, density, effective heat capacity, and thermal conductivity of the base liquid, respectively, whereas $\boldsymbol{\phi}$ is the nanoparticle volumetric fraction coefficient. Furthermore, $\boldsymbol{\rho_s}$, $\boldsymbol{(C_p)_s}$, and $\boldsymbol{\kappa_s}$ are the density, adequate heat capacity, and thermal conductivity of the nanoparticles, respectively. The mutable current conductivity is expressed by the following structure:

$$\boldsymbol{\kappa^*_{nf}(¥) = k_{nf}\left[1 + \epsilon\frac{T - T_\infty}{T_w - T_\infty}\right]} \quad (6)$$

2.3. Nanoparticles and Base Fluid Features

Table 2 lists the chemical and physical parameters of the engine oil and several nanoparticles employed in this research.

Table 2. Principal properties of the base fluid and nanoparticles at a standard temperature [59,60].

Thermophysical Properties	$\boldsymbol{\rho}$(kg/m^3)	$\boldsymbol{c_p}$(J/kgK)	$\boldsymbol{k}$(W/mK)
SWCNT	2600	425	6600
MWCNT	1600	796	3000
CMC	997.10	4179	0.6130

2.4. Roseland Approximations

The Roseland approximation [61], as in Equation (7), is used to represent the radiation parameter in Equation (4).

$$\boldsymbol{q_r} = -\frac{\boldsymbol{4\sigma^*}}{\boldsymbol{3k^*}}\frac{\boldsymbol{\partial ¥^4}}{\boldsymbol{\partial y}} \tag{7}$$

In this study, $\boldsymbol{\sigma^*}$ indicates the Stefan–Boltzmann value, and $\boldsymbol{k^*}$ represents the captivation coefficient.

3. Numerical Solution

By using the similarity approach, BVP (2)–(5) are transformed into ordinary differential equations (ODE). The stream functions ($\boldsymbol{\psi}$) are introduced as:

$$\boldsymbol{u} = \boldsymbol{\psi_y}, \boldsymbol{v} = -\boldsymbol{\psi_x}, \tag{8}$$

The similarity variables are expressed as:

$$\boldsymbol{\Upsilon(x,y)} = \sqrt{\frac{\boldsymbol{b}}{\boldsymbol{\nu_f}}}\boldsymbol{y}, \boldsymbol{\psi(x,y)} = \sqrt{\boldsymbol{\nu_f b}}\boldsymbol{xf(\Upsilon)}, \boldsymbol{\theta(\Upsilon)} = \frac{¥ - ¥_\infty}{¥_w - ¥_\infty}, \tag{9}$$

Then, according to (2)–(4), the following equations are obtained:

$$\left.\begin{array}{c} \boldsymbol{f''' + \phi_1[\phi_2(ff'' - f'^2) + \beta_1(2f'f''' - ff^{iv}) + 3(\beta_1 + \beta_2)f''^2]} \\ \boldsymbol{+6\phi_1\beta_3 R_e f''^2 f''' - Kf' = 0,} \end{array}\right\} \tag{10}$$

$$\boldsymbol{\theta''\left(1 + \epsilon\theta + \frac{1}{\phi_4}P_r N_r\right) + \epsilon\theta'^2 + P_r\frac{\phi_3}{\phi_4}\left[f\theta' - f'\theta + \theta\frac{Q_r}{\phi_3} + \frac{E_c}{\phi_1\phi_3}f''^2\right] = 0,} \tag{11}$$

with

$$\left.\begin{array}{l} \boldsymbol{f(0) = S, f'(0) = 1 + \Lambda f''(0), \theta'(0) = -B_ç(1 - \theta(0))} \\ \boldsymbol{f'(\Upsilon) \to 0, f''(\Upsilon) \to 0, \theta(\Upsilon) \to 0, as\ \Upsilon \to \infty.} \end{array}\right\} \tag{12}$$

where $\boldsymbol{\phi'_i s}$ is $\boldsymbol{1 \le i \le 4}$ in Equations (10) and (11). The thermophysical characteristics of the third-grade nanofluid are shown below.

$$\left.\begin{array}{l} \boldsymbol{\phi_1 = (1 - \phi)^{2.5}, \phi_2 = \left(1 - \phi + \phi\frac{\rho_s}{\rho_f}\right), \phi_3 = \left(1 - \phi + \phi\frac{(\rho C_p)_s}{(\rho C_p)_f}\right)} \\ \boldsymbol{\phi_4 = \left(\frac{(k_s + 2k_f) - 2\phi(k_f - k_s)}{(k_s + 2k_f) + \phi(k_f - k_s)}\right).} \end{array}\right\} \tag{13}$$

3.1. Description of the Embedded Control Physical Parameters

Therefore, (2) is fulfilled. According to the derivative with respect to $\boldsymbol{\Upsilon}, \boldsymbol{\beta_1} = \frac{\boldsymbol{b\lambda_1}}{\boldsymbol{\mu_f}}$, $\boldsymbol{\beta_2} = \frac{\boldsymbol{b\lambda_2}}{\boldsymbol{\mu_f}}$ and $\boldsymbol{\beta_3} = \frac{\boldsymbol{b\lambda_3}}{\boldsymbol{\mu_f}}$, which represent the material parameters of the third-grade fluid and $\boldsymbol{K} = \frac{\boldsymbol{\nu_f}}{\boldsymbol{b\kappa_f}}$, respectively. $\boldsymbol{P_r} = \frac{\boldsymbol{\nu_f}}{\boldsymbol{\alpha_f}}$ is the Prandtl value. Thermal diffusivity parameter, heat source, mass transfer parameter, and thermal radiation parameter are represented by $\boldsymbol{\alpha_f} = \frac{\boldsymbol{\kappa_f}}{\boldsymbol{(\rho C_p)_f}}$, $\boldsymbol{S} = -\boldsymbol{V_w}\sqrt{\frac{\boldsymbol{1}}{\boldsymbol{\nu_f b}}}$, and $\boldsymbol{N_r} = \frac{\boldsymbol{16}}{\boldsymbol{3}}\frac{\boldsymbol{\sigma^* T_\infty^3}}{\boldsymbol{\kappa^* \nu_f (\rho C_p)_f}}$, respectively. $\boldsymbol{Q_r} = \frac{\boldsymbol{Q_0}}{\boldsymbol{(\rho C_p)_f b}}$ and $\boldsymbol{\Lambda} = \sqrt{\frac{\boldsymbol{b}}{\boldsymbol{\nu_f}}}\boldsymbol{N_L}$ are the heat source and velocity slip parameter, respectively. $\boldsymbol{E_c} = \frac{\boldsymbol{U_w^2}}{\boldsymbol{(C_p)_f(T_w - T_\infty)}}$ and $\boldsymbol{B_ç} = \frac{\boldsymbol{h_f}}{\boldsymbol{k_0}}\sqrt{\frac{\boldsymbol{\nu_f}}{\boldsymbol{b}}}$ are the Eckert and Biot numbers, respectively.

3.2. Convective Rate of HT: Nusselt Number

The flow is controlled by the local Nusselt number ($\boldsymbol{Nu_x}$) [62], which may be expressed as a physical quantity as follows:

$$\boldsymbol{Nu_x} = \frac{\boldsymbol{xq_w}}{\boldsymbol{k_f(¥_w - ¥_\infty)}} \tag{14}$$

where $\boldsymbol{q_w}$ epitomizes the heat flux resolute by:

$$\boldsymbol{q_w} = -\boldsymbol{k_{nf}}\left(\mathbf{1} + \frac{\mathbf{16}}{\mathbf{3}}\frac{\boldsymbol{\sigma^* ¥_\infty^3}}{\boldsymbol{\kappa^* \nu_f(\rho C_p)_f}}\right)\left(¥_y\right)_{\boldsymbol{y=0}}. \tag{15}$$

The non-dimensional transformations (9) are applied to afford:

$$\boldsymbol{Nu_x Re_x^{-\frac{1}{2}}} = -\frac{\boldsymbol{k_{nf}}}{\boldsymbol{k_f}}(\mathbf{1} + \boldsymbol{N_r})\boldsymbol{\theta'}(\mathbf{0}), \tag{16}$$

where $\boldsymbol{Nu_x}$ is the Nusselt number, and $\boldsymbol{C_f}$ represents the reduced skin friction. $\boldsymbol{Re_x} = \frac{\boldsymbol{U_w x}}{\boldsymbol{\nu_f}}$ is the local $\boldsymbol{Re}$, contingent upon the broadening velocity, $(\boldsymbol{U_w(x)})$.

4. Irreversibility Analysis

The Entropy lifetime [63] for the suppositions, as previously mentioned, is:

$$\boldsymbol{E_G} = \frac{\boldsymbol{k_{nf}}}{\boldsymbol{T_\infty^2}}\left\{\left(¥_y\right)^2 + \frac{\mathbf{16}}{\mathbf{3}}\frac{\boldsymbol{\sigma^* T_\infty^3}}{\boldsymbol{\kappa^* \nu_f(\rho C_p)_f}}\left(¥_y\right)^2\right\} + \frac{\boldsymbol{\mu_{nf}}}{\boldsymbol{T_\infty}}\left(\boldsymbol{u_y}\right)^2 + \frac{\boldsymbol{\mu_{nf} u^2}}{\boldsymbol{kT_\infty}}. \tag{17}$$

The dimensionless formula of the entropy equation is expressed as:

$$\boldsymbol{N_G} = \frac{¥_\infty{}^2 \boldsymbol{b^2 E_G}}{\boldsymbol{k_f}(¥_w - ¥_\infty)^2}. \tag{18}$$

Based on (9), the following expression is obtained:

$$\boldsymbol{N_G} = \boldsymbol{R_e}\left[\boldsymbol{\phi_4}(\mathbf{1} + \boldsymbol{N_r})\boldsymbol{\theta'^2} + \frac{\mathbf{1}}{\boldsymbol{\phi_1}}\frac{\boldsymbol{B_r}}{\boldsymbol{\Omega}}(\boldsymbol{f''^2} + \boldsymbol{Kf'^2})\right]. \tag{19}$$

5. Numerical Implementation: Galerkin Finite Element Method

Numerical computations are utilized to resolve mathematical models (10), (11), and (12). The G-FEM implementation is outlined as follows.

- The residuals for problems (10)–(12) are weighted, and integrals are taken over the typical element in their written form;
- In order to obtain the weak systems, the linear second-order derivative expressions are integrated;
- Galerkin approximations are utilized to estimate the weak systems, and stiffness elements are produced according to those results;
- The nonlinear system is assembled using the forcing vectors and boundary vectors of the stiffness elements;
- The Picard linearization approach is used to linearize the nonlinear system, and the Gauss–Seidel procedure is used to solve the linearized problem repeatedly;
- Furthermore, convergence analysis is accomplished by ensuring that the obtained values are mesh-free.

Examples of the parametric research are provided to demonstrate the effects of porous media, variable thermal conductivity, thermal radiation, heat source, viscous dissipation, and the rate of heat flow on the study of thermal energy in 2D non-Newtonian third-grade fluid flow. Table 3 shows 300-element mesh-free analysis results. Furthermore, a flow chart of the Galerkin finite element technique is depicted in Figure 2.

Table 3. Velocities and temperatures based on a 300-element grid.

No. of Elements	$f'\left(\frac{\Upsilon_{max}}{2}\right)$	$\theta\left(\frac{\Upsilon_{max}}{2}\right)$
30	0.0326964105	0.00543392174
60	0.3008137336	0.00482355489
90	0.2787224963	0.00452597831
120	0.2518385629	0.00423211689
150	0.2327463208	0.00396988127
180	0.2164459730	0.00357315905
210	0.1902813462	0.00327698245
240	0.1907921025	0.00305766541
270	0.1906827572	0.00274452730
300	0.1905266081	0.00253240956

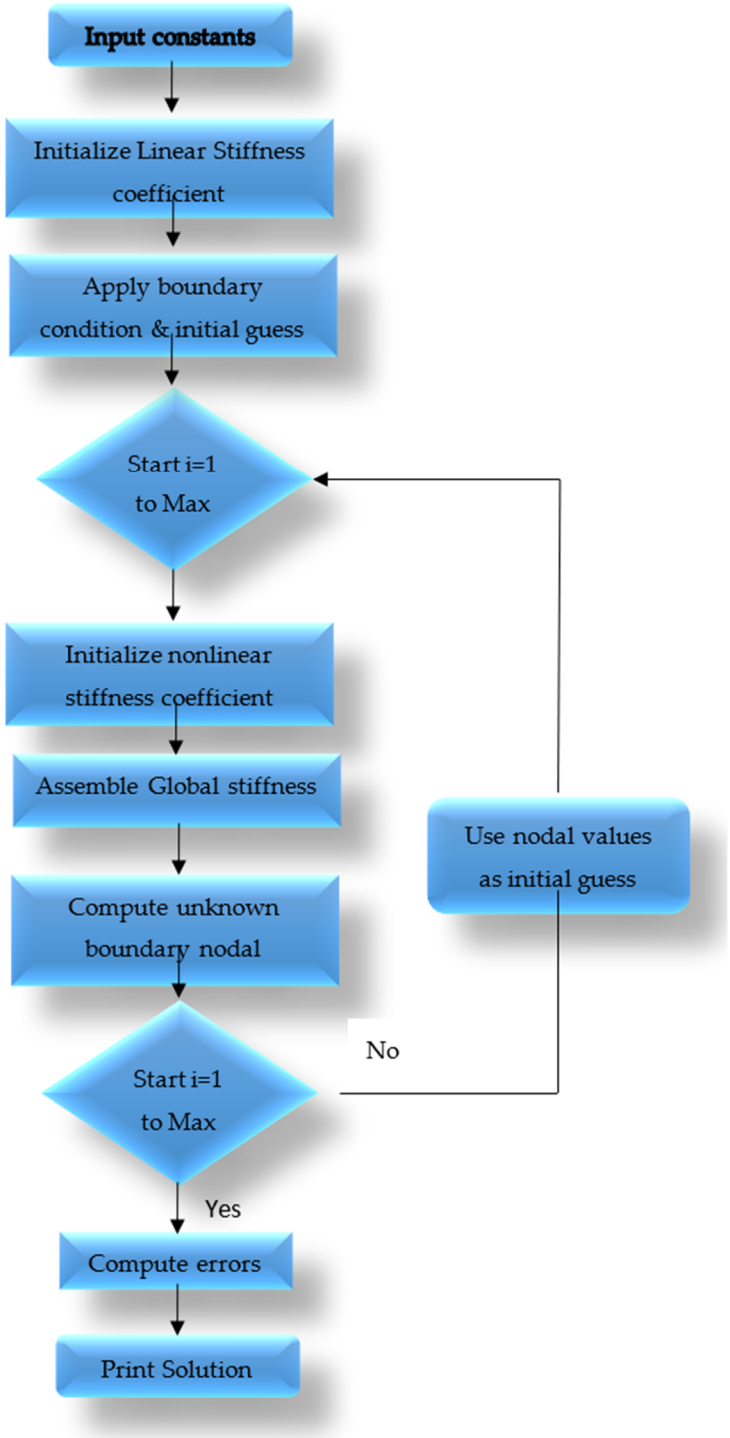

Figure 2. Flow chart of the Galerkin finite element technique.

6. Validity of Code

The reported findings we verified by comparison with previously published outcomes [64,65]. Each value in Table 4 was independently verified in the interest of reliability. According to dissimilarity, the current findings are consistent and widely recognized.

Table 4. Assessment of $-\theta'(0)$ for various P_r values, where $\boldsymbol{\phi} = 0$, $\boldsymbol{\epsilon} = 0$, $\boldsymbol{\Lambda} = 0$, $\boldsymbol{N_r} = 0$, $\boldsymbol{Q_r} = 0$, $\boldsymbol{Ec} = 0$, $\boldsymbol{S} = 0$, and $\boldsymbol{B_\varsigma} \to 0$.

Pr	**Ref. [64]**	**Ref. [65]**	**Present**
0.72	0.80876181	0.80876181	0.80876184
1.0	1.0	1.0	1.0
3.0	1.92357420	1.92357420	1.92357418
7.0	3.07314651	3.07314651	3.07314650
10.0	3.72055429	3.72055429	3.72055422

7. Results and Discussion

In permeable radiation nanofluid studies, variable thermal conductivity, viscosity dissipation, and unstable boundary conditions are investigated. The following discourse depends primarily on generated numerical and graphical findings acquired using the Galerkin finite element technique. The outcomes of physical parameters are denoted as $\boldsymbol{\beta_1}$, $\boldsymbol{\beta_2}$, $\boldsymbol{\beta_3}$, $\boldsymbol{K}$, $\boldsymbol{\phi}$, $\boldsymbol{\Lambda}$, $\boldsymbol{\epsilon}$, $\boldsymbol{N_r}$, $\boldsymbol{E_c}$, $\boldsymbol{Q_r}$, $\boldsymbol{B_\varsigma}$, $\boldsymbol{S}$, $\boldsymbol{R_e}$, and $\boldsymbol{B_r}$. The numerical results were obtained are using SWCNT-CMC and MWCNT-CMC as non-Newtonian third-grade nanofluids. The decency of the speed, temperature and entropy generations difference are depicted in Figures 3–25. For simplicity, several parameters are assigned to constant values, such as $\boldsymbol{\beta_1} = \boldsymbol{0.1}$, $\boldsymbol{\beta_2} = \boldsymbol{0.3}$, $\boldsymbol{\beta_3} = \boldsymbol{0.5}$, $\boldsymbol{K}$= 0.2, $\boldsymbol{\phi}$ = 0.1, $\boldsymbol{\Lambda}$ = 0.2, $\boldsymbol{\epsilon}$ = 0.1, $\boldsymbol{N_r}$ = 0.1, $\boldsymbol{E_c}$= 0.2, $\boldsymbol{Q_r}$ = 0.3, $\boldsymbol{B_\varsigma} = \boldsymbol{0.1}$, $\boldsymbol{S} = \boldsymbol{0.1}$, $\boldsymbol{R_e} = \boldsymbol{5}$, and $\boldsymbol{B_r} = \boldsymbol{5}$.

7.1. Effect of Deborah Numbers ($\boldsymbol{\beta_1}$) and ($\boldsymbol{\beta_2}$)

A Deborah number is a dimensionless number that is frequently used in rheology to describe the fluidity of substances under particular flow conditions. Material behavior enters a non-Newtonian phase with significant Deborah numbers when elasticity progressively dominates and solid-like behavior is observed. Figure 3 illustrates the velocity of both nanofluids with varying $\boldsymbol{\beta_1}$ values (for basic fluid). The velocity of the flow for both kinds of nanofluids is reduces as the value of $\boldsymbol{\beta_1}$ is increased because the basic fluid is easily influenced by $\boldsymbol{\beta_1}$. However, according to observation, MWCNT-CMC has a higher velocity than that of SWCNT-CMC.

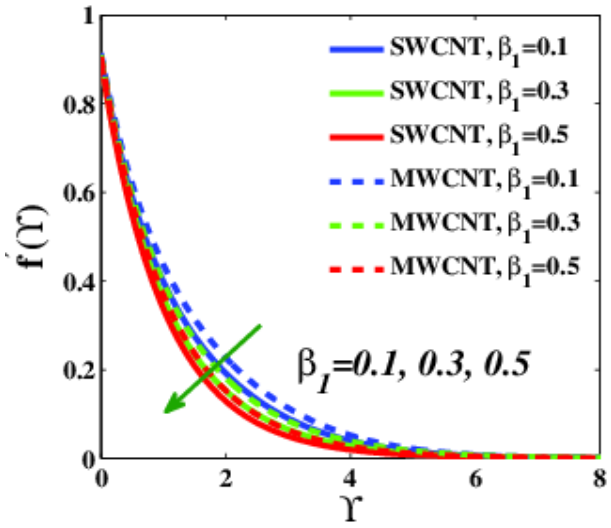

Figure 3. Velocity variation versus $\boldsymbol{\beta_1}$.

Therefore, the momentum boundary layer thickness of MWCNT-CMC is increased. The consequence of reduced velocity is shown in Figure 4. Figure 4 shows the effect of changes in $\boldsymbol{\beta_1}$ on the temperature profile for both nanofluids. The thermal distribution increased with increased $\boldsymbol{\beta_1}$ values. This anomaly occurs due to the slowing down of the

movement of the nanomolecules in the liquid, resulting in reduced heat transfer from the shallow end in the direction of the movement, which eventually increased the heat transfer temperature. The temperature of MWCNT-CMC is slightly higher than that of SWCNT-CMC because SWCNT is a better heat conductor than MWCNT.

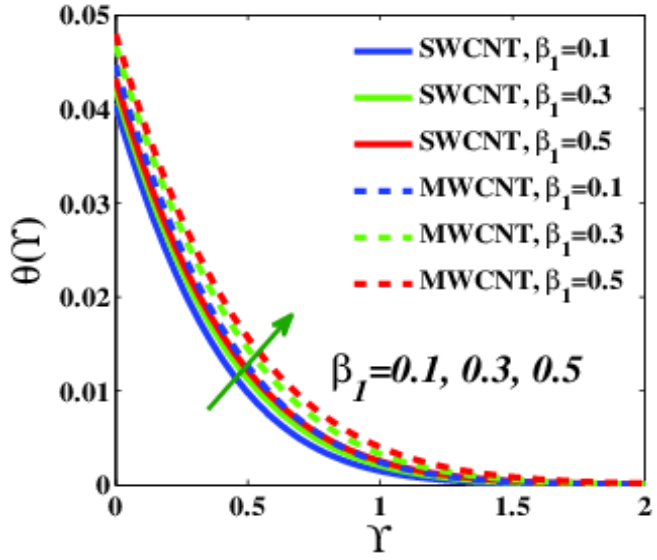

Figure 4. Temperature variation versus $\boldsymbol{\beta_1}$.

Figure 5 shows the velocity distribution when the third-grade parameter, $\boldsymbol{\beta_2}$ (for nanoparticles), is reinforced, indicating a dramatic increase in fluid velocity. This phenomenon lead an increased width of the momentum boundary layer. Nonetheless, MWCNT-CMC has a higher velocity than that of SWCNT-CMC. However, the viscosity does not affect MWCNT-CMC under these conditions. The fluid thickness can be reduced by adjusting the third-grade parameter, which is well-known for this purpose.

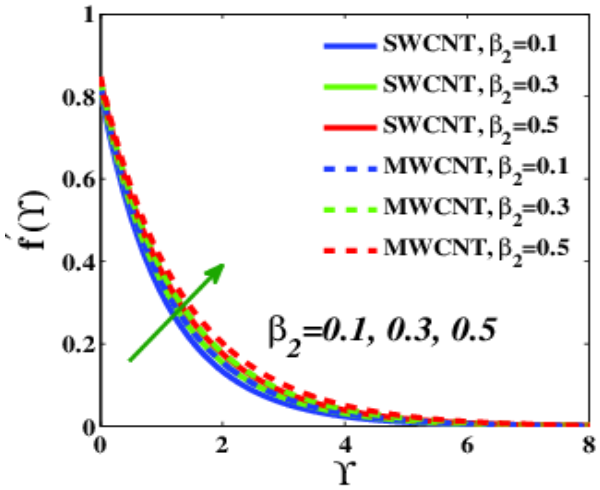

Figure 5. Velocity variation versus $\boldsymbol{\beta_2}$.

Figure 6 depicts the varying patterns of heat dispersion. An increase in temperature causes a reduction in the diffusion of thermal energy, resulting in a reduction in the width of the thermal boundary layer. These results demonstrate that temperature from the shallow velocity is rapidly transferred to the fluid and emitted into the distant field. This phenomenon occurs because the fluid's velocity increases as it moves through the system. SWCNT-CMC has a lower temperature relative to that of other nanofluids because SWCNT is a good heat conductor. Similarly, the velocity for the third-grade parameter,

$\boldsymbol{\beta_3}$, increases as the parameter increases, as illustrated in Figure 7. The figure shows that MWCNT-CMC has a higher velocity than that of SWCNT-CMC. The fluid boundary thickness is reduced when SWCNT-CMC is used as a nanofluid, which acceptable because MWCNT-CMC has a more negligible effect on the third-grade parameter, $\boldsymbol{\beta_3}$.

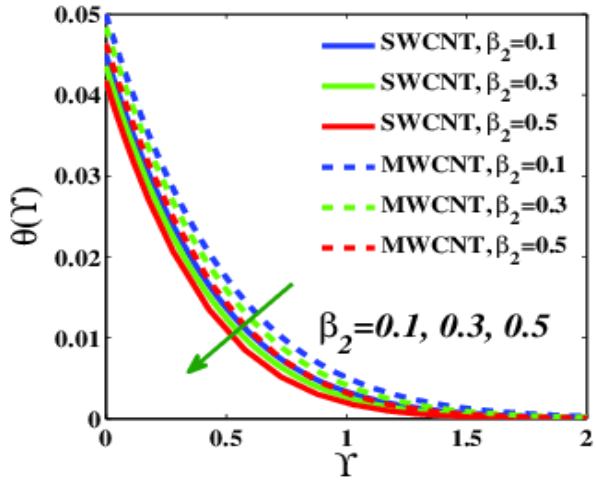

Figure 6. Temperature variation versus $\boldsymbol{\beta_2}$.

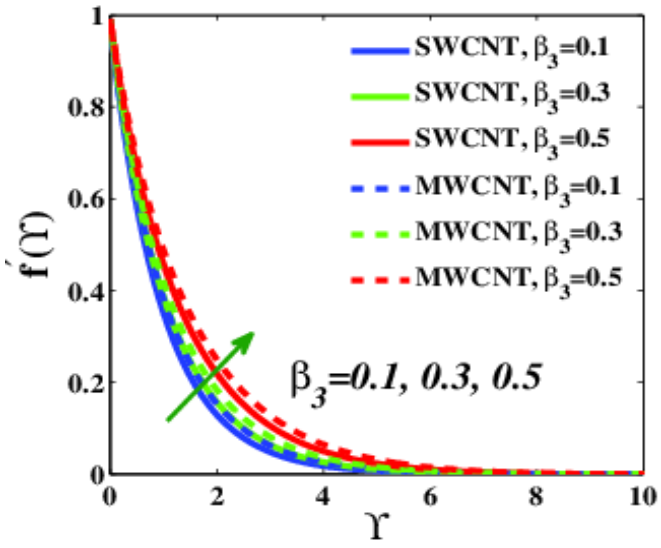

Figure 7. Velocity variation versus $\boldsymbol{\beta_3}$.

7.2. Effect of Porous Media Parameter ($\boldsymbol{K}$)

To the best of our knowledge, the porosity of a material ($\boldsymbol{K}$) can be calculated by subtracting the density from the void percentage. It is well-known that the system's skin friction coefficient is affected by porosity. Figure 8 demonstrates the importance of porosity near the velocity profile for both nanofluid types. The increased porosity was verified in both fluids, as indicated above. The increase in velocity is the result of the reduction in the value of $\boldsymbol{K}$. These circumstances occur because the friction between the movement and the shallow velocity is an annexed, resulting in reduced velocity. Increased porosity can be applied in order to reduce the friction between the surface plate and the nanofluid molecules. However, SWCNT-CMC moves slower than other nanofluids, although the momentum boundary is thinner for SWCNT-CMC than MWCNT-CMC. As the material's porosity increases, so does the temperature profile for both nanofluids. Furthermore, the temperature is reduced with a lower porous media parameter value. Figure 9 show this trend for both types of nanofluids. Owing to the porosity of the material, the fluid is

sucked into the surface. Consequently, the temperature profile of SWCNT-CMC is reduces, as shown in Figure 4. It is worthwhile to investigate the entropy of the system in conjunction with the influence of the porous media parameter in the system. Figure 10 depicts the heightened entropy in the system as a result of the absence of temperature transfer in the system. This occurrence is likely to emerge as a result of reduced velocity, causing heat transfer to be delayed in the system and resulting in accumulated entropy.

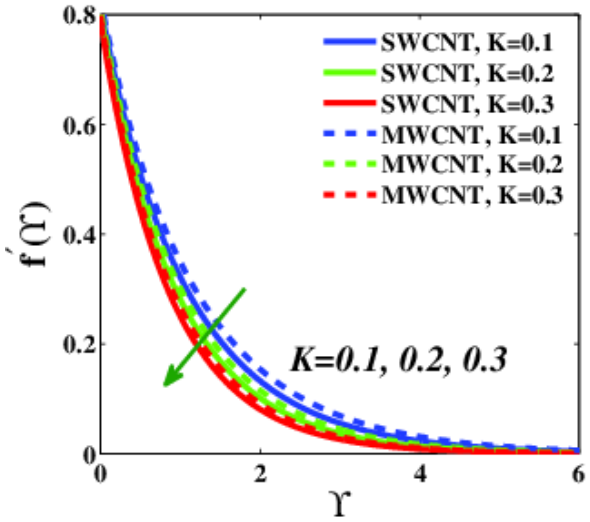

Figure 8. Velocity variation versus ***K***.

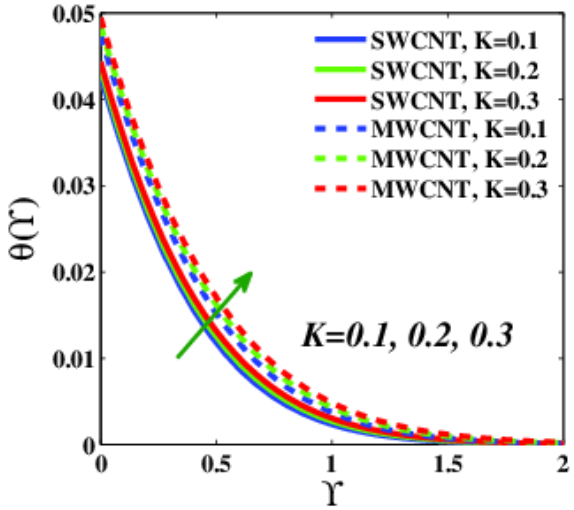

Figure 9. Temperature variation versus ***K***.

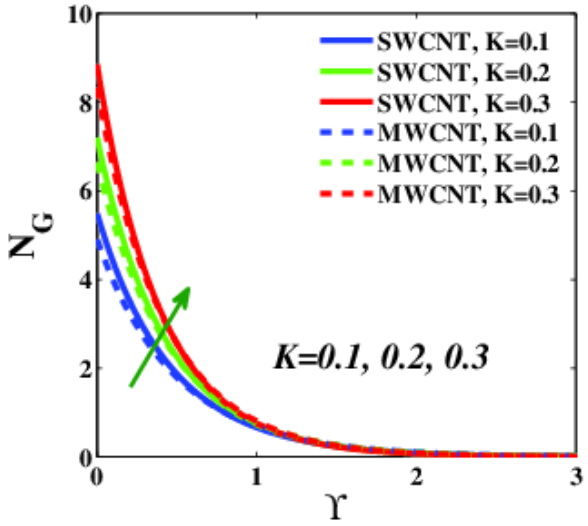

Figure 10. Entropy variation versus $\boldsymbol{K}$.

7.3. The Influence of Volume Fraction Nanoparticle Parameter ($\boldsymbol{\phi}$)

The volume concentration and volume fraction are the same in ideal solutions when the volumes of all of the constituents are added together (the volume of the solution is equal to the sum of the volumes of its ingredients). Prior to mixing, the volume fraction of a specific element (metal nanoparticle) is calculated by dividing the volume of that component (metal nanoparticle) by that of the mixture (basic fluid). The effect of the nanoparticle volume fraction parameter on particle velocity is shown in Figure 11. The speed of the fluid dynamics diminishes as the volume fraction of the nanoparticles of both nanofluids increases. This phenomenon occurs as a result of the aggregate fluid viscosity of the amassed nanofluid concentration, increasing the friction. As a result of this increase, the MWCNT-CMC nanofluid has a higher velocity that that of the SWCNT-CMC nanofluid. Furthermore, the system temperature increase, along with ϕ, as shown in Figure 12. Liquid velocity plays an active role in HT. When the mobility of the particles in the fluid is slowed, heat accumulates in the system. As a consequence, the system temperature doubles. Additionally, the entropy of the system is expected to intensify, owing to the increased temperature, as shown in Figure 1. The numerical results presented in Figure 13 reveal that the volume percentage of nanoparticles has a substantial influence on the generated entropy. A comparison of the two nanofluids, reveals that the MWCNT-CMC nanofluid creates less entropy than the SWCNT-CMC nanofluid, as shown in Figure 13. This discovery suggests that MWCNT-CMC nanofluids are superior to SWCNT-CMC nanofluids in terms of controlling the system entropy.

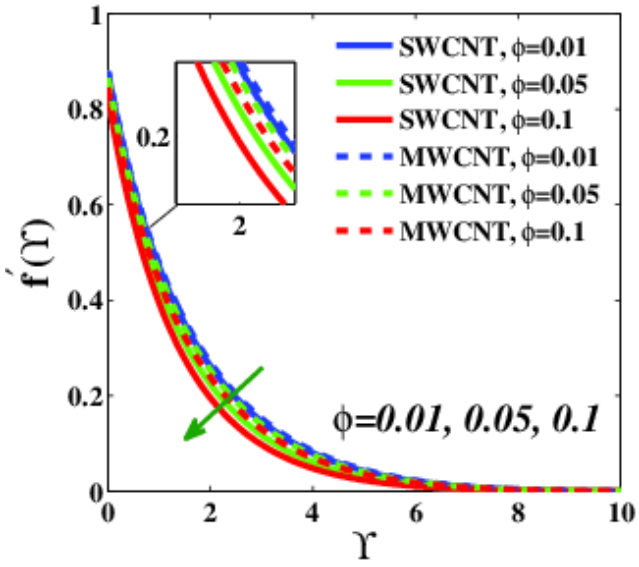

Figure 11. f' variation versus ϕ.

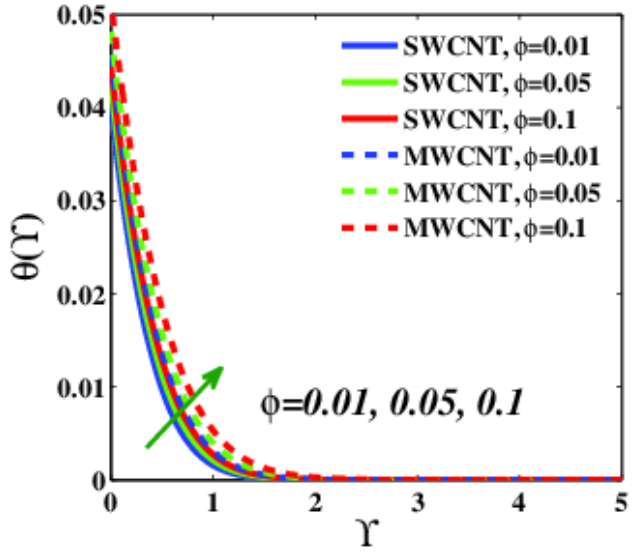

Figure 12. Temperature variation versus ϕ.

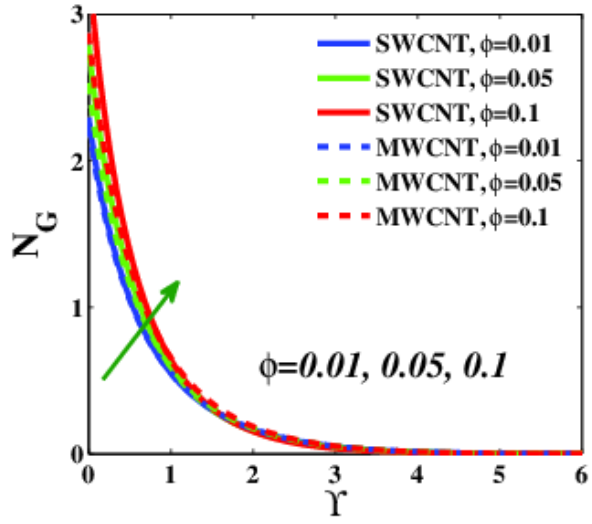

Figure 13. Entropy variation versus ϕ.

*7.4. The Influence of Velocity Slip Parameter (**Λ**)*

The velocity slip parameter describes the difference in movement between the transporting air and the discharged particles. The velocity slip condition is determined along the walls. As shown in Figure 14, the velocity slip parameter prompts the flow rate to accelerate. This phenomenon arises because the slip enhances the frictional resistance between the current and the shallow entropy. The velocity of the MWCNT-CMC nanofluid is higher than that of the SWCNT-CMC NF because the NF contains metal particles (MWCNT) with a strong link that is difficult to disrupt. Due to the lower velocity, the heat of the movement expands as the velocity slip increases, as shown in Figure 15, occurring as a natural result of less heat being transmitted from one spot to another. Although MWCNT-CMC NF moves faster than SWCNT-CMC, the heat profile for SWCNT-CMC is lower than that of MWCNT-CMC because SWCNT nanoparticles are better heat conductors than MWCNT nanoparticles. The heat is transferred faster through SWCNT nanoparticles from the surface to the flow, passing toward the far field. The system entropy reduces as the velocity slip proliferates, as shown in Figure 16, because MWCNT and SWCNT nanoparticles have more significant positive enthalpies, allowing for the bonding dynamism and operational atoms that protect against increased entropy. Furthermore, the physical molecules of MWCNT nanoparticles have less entropy than SWCNT nanoparticles in the system, indicating that MWCNT nanoparticles have stronger bonding for energy and atoms, making it difficult to increase the entropy.

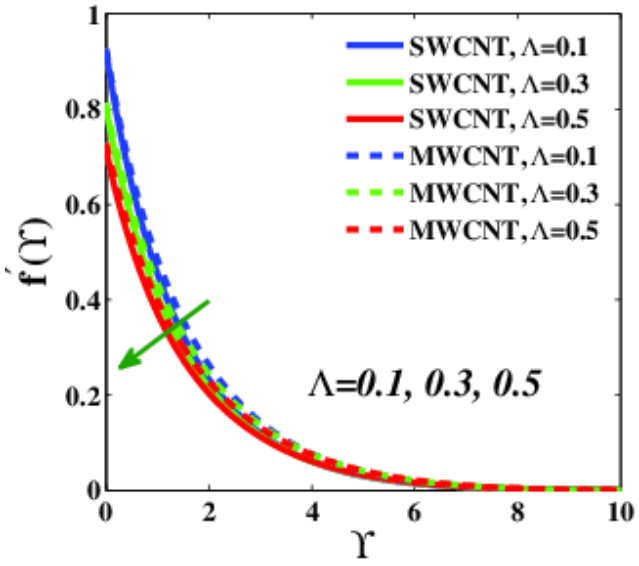

Figure 14. Velocity variation versus **Λ**.

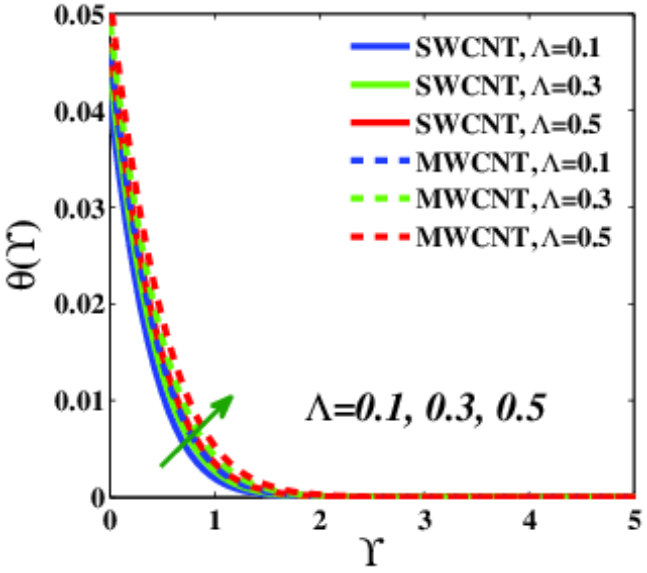

Figure 15. Temperature variation versus **Λ**.

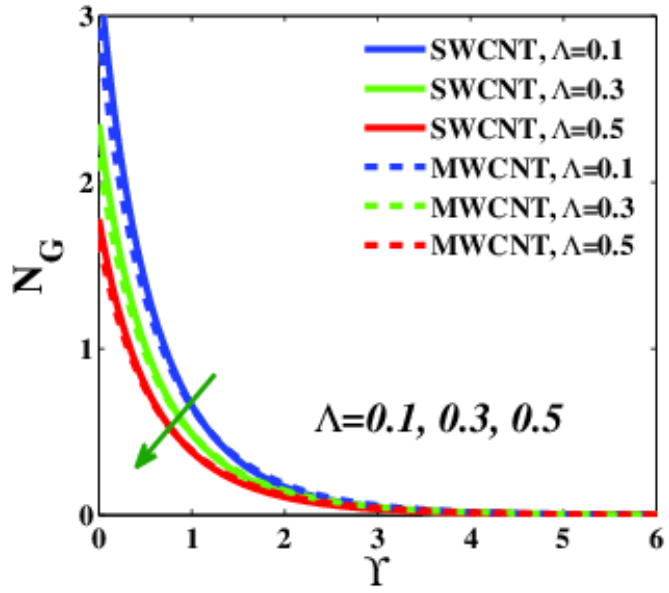

Figure 16. Entropy variation versus **Λ**.

7.5. Effect of Biot Number ($\boldsymbol{B_\varsigma}$), Variable Thermal Conductivity ($\boldsymbol{\varepsilon}$), and Radiation Parameter ($\boldsymbol{N_r}$)

The Biot Number denotes the ratio of heat conduction resistance to heat convection resistance in a solid mass. The resistance between the body and its surroundings illustrates how temperature fluctuates from the mass core to the atmosphere. The effect of the Biot number on the flow temperature shown in Figure 17, with the chart indicating that the temperature increases with increased Biot number. This striking pattern demonstrates that the thermal resistances inside the flow are amplified, magnifying the flow temperature. The temperature profile of MWCNT-CMC is higher than that of SWCNT-CMC due to the superior heat performance of SWCNT. The ability of a substance to carry heat is measured by its thermal conductivity. Low-thermal-conductivity materials have a lower rate of HT than high-thermal-conductivity materials. Figure 18 demonstrates the effectiveness of the variable thermal conductivity parameter with respect to the temperature profile. The higher the thermal conductivity, the higher the temperature of both nanofluids, which explains the reduced rate of heat transmission of both nanofluids. Howbeit, the

temperature of SWCNT-CMC is still higher than that of MWCNT-CMC because SWCNT is a better heat conductor than MWCNT. Figure 19 illustrates the radiation response caused by the heat exchange between the flow and its surroundings (far-field). The illustration shows that the ambient temperature influences the amplified flow temperature. This phenomenon is caused by the environment and the flow attempting to reach an equilibrium state. The ambient temperature is more sophisticated than the temperature of the flow. As a result, the flow temperature increases, as shown in Figure 19. SWCNT-CMC is therefore proven to be a better heat conductor than MWCNT-CMC, as SWCNT-CMC has a lower temperature profile, emphasizing that the energy in the system is irreversibly transformed.

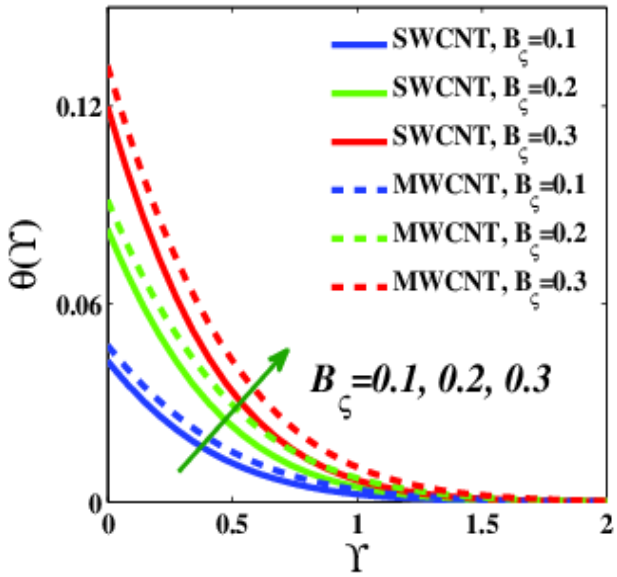

Figure 17. Temperature variations versus B_{ς}.

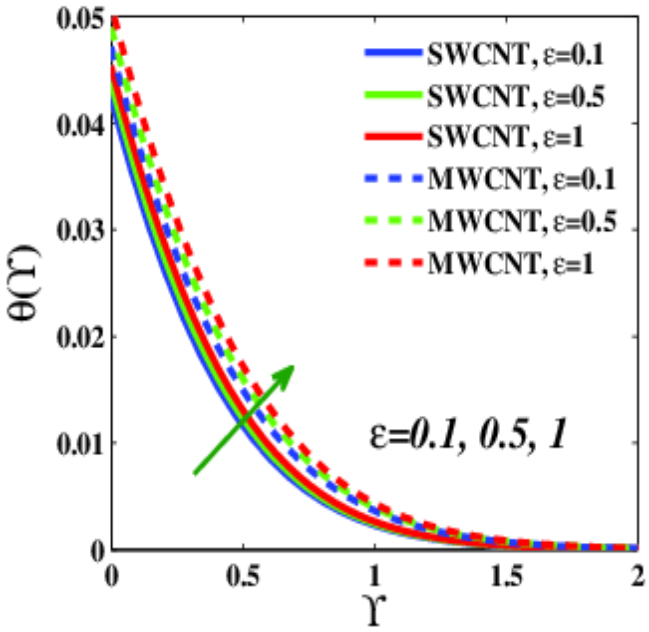

Figure 18. Temperature variations versus ε.

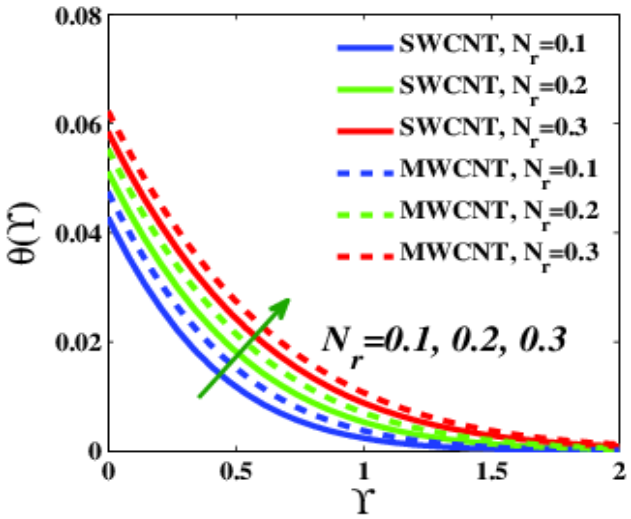

Figure 19. Temperature variations versus $\boldsymbol{Nr}$.

7.6. Effect of the Suction ($\boldsymbol{S > 0}$)/Injection ($\boldsymbol{S < 0}$) Parameter

Suction and injection parameters must be analyzed in terms of their impact on the flow. Figure 20 shows that when suction proliferates, the flow velocity is reduced. The suction action disrupts the flow on the surface. Consequently, the flow velocity depreciates over time. The momentum of the SWCNT-CMC is reduced at the beginning of the process. However, it gains speed after reaching a threshold value because SWCNT-CMC molecules are much smaller than MWCNT-CMC molecules, making it is easier for SWCNT-CMC to move around with under the suction impact of the system. However, as shown in Figure 21, the suction effect significantly reduces the flow temperature. Due to the surface porosity, the speed of the top layer increases, and the flow is drawn into the hole by the porosity. Increased cooling of the flow is made possible by the rapid transmission of heat. SWCNT-CMC has been shown to be a more efficient heat conductor than MWCNT-CMC due to its lower temperature profile. However, this conclusion has the consequence of expanding the system entropy. Figure 22 shows than an increase in the injection parameter increases the fluid velocity because the flow is injected or boosted up to an inner layer, resulting in an increase in the overall flow velocity. This result shows that MWCNT-CMC is much faster than SWCNT-CMC with respect to the injection effect, possibly because the MWCNT-CMC moves more easily when it is pushed, whereas SWCNT-CMC has more difficulties moving. A secondary consequence of the increased injection parameter is an increase in the flow temperature. Figure 23 clearly shows this outcome. The graphic shows how changing the injection parameter increases the flow temperature. However, the injection parameter does not have a noticeable effect on SWCNT-CMC, as this nanofluid is a better heat conductor than MWCNT-CMC. Despite the escalation in entropy, the system entropy decreases because the surface lacks porosity, making it easier for the system to regulate the flow of energy.

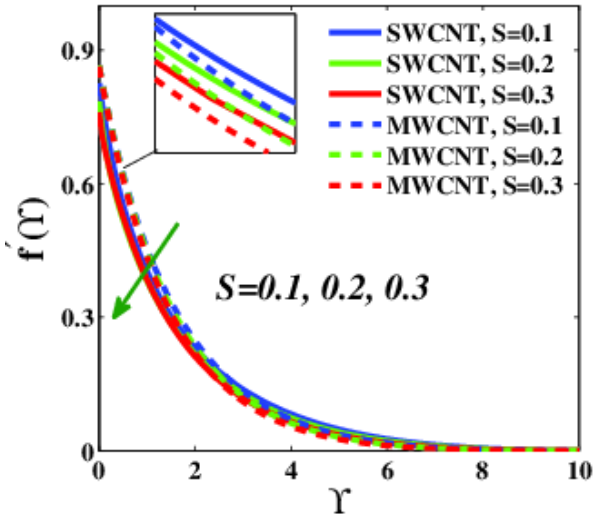

Figure 20. Velocity variations versus $S > 0$.

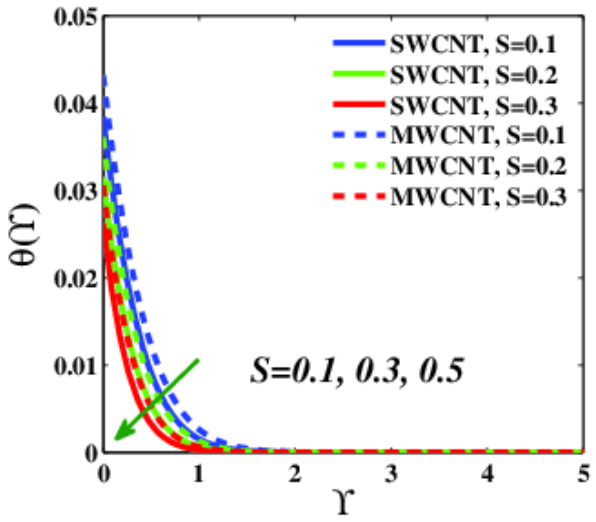

Figure 21. Temperature variations versus $S > 0$.

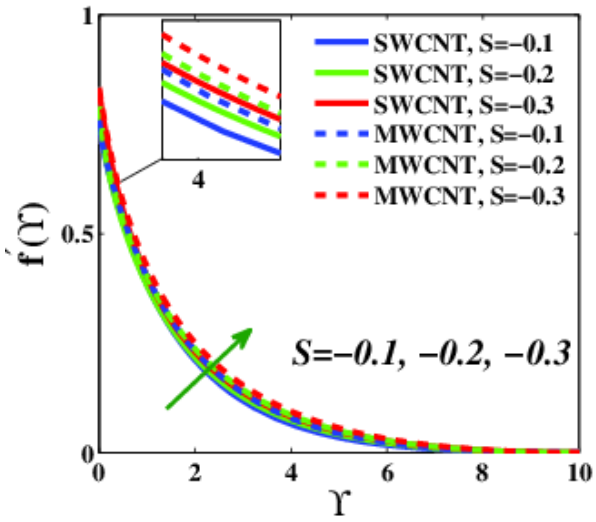

Figure 22. Velocity variations versus $S < 0$.

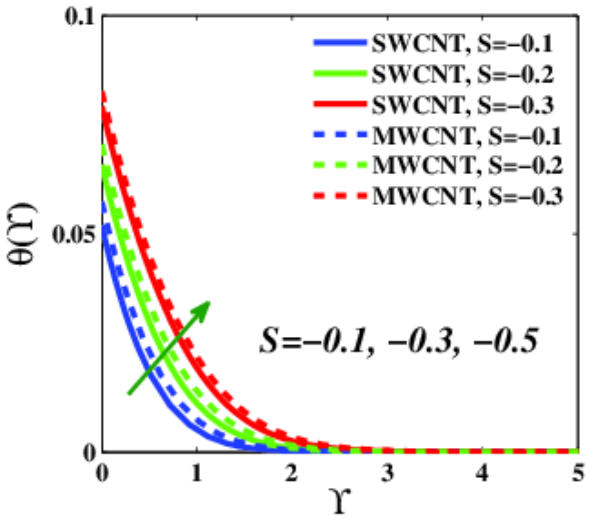

Figure 23. Temperature variations versus $S < 0$.

7.7. Impact of Reynolds Number (R_e) and Brinkman Number (B_r) on Entropy Generation

As shown in Figure 24, the entropy of a system reduces as the Reynold number increases due to increased inertial forces in the system. The particles in the hybrid nanofluid have high kinetic energy, which leads them to move more quickly and exhibit a high Reynold number. The fact that MWCNT-CMC nanofluid has a lower entropy value than SWCNT-CMC is surprising. MWCNT has a far greater affinity for basic fluids than SWCNT. As a result, entropy is unable to cause a rapid breakdown of the system. The impact of the Brinkman number is visually appealing because it depicts the ratio of heat produced by viscous dissipation to heat conveyed by molecular transference. As shown in Figure 25, the Brinkman number expends the system's entropy generation. The generated heat is mainly a result of viscous dissipation. Furthermore, MWCNT-CMC lower entropy than SWCNT-CMC nanofluid. MWCNT has a far greater affinity for aqueous solutions than SWCNT. As a result, entropy is unable to rapidly destabilize the system.

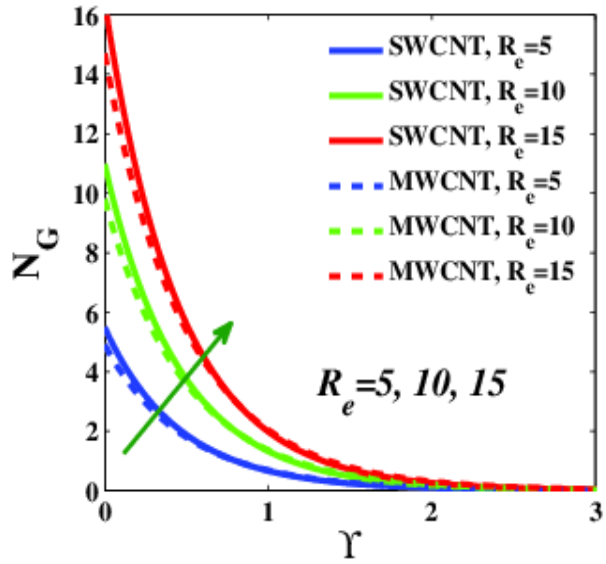

Figure 24. Entropy variations versus Re.

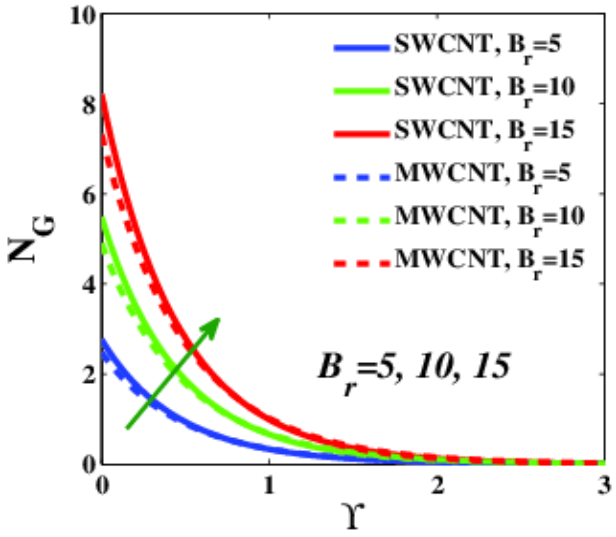

Figure 25. Entropy variations versus $\boldsymbol{Br}$.

7.8. Relative HT Rate in SWCNT-CMC and MWCNT-CMC Nanofluids

Owing to its higher thermal conductivity relative to MWCNT, SWCNT provides a superior substrate for heat transmission in nanofluids, improving heat conduction. Table 5 shows the Nusselt number results. The Biot number increases both nanofluids, but MWCNT-CMC transmits more heat than SWCNT-CMC because MWCNT-CMC is a better heat conductor than SWCNT-CMC. In contrast, the velocity slip deteriorates the heat transmission for both nanofluids. In terms of heat transmission with respect to this parameter is slightly more reduced for SWCNT-CMC than MWCNT-CMC. Both nanofluids are reduced with respect to this parameter. Moreover, the suction parameter can aggravate the heat transmission for both nanofluids. It is expected that the heat transmission for MWCNT-CMC is better than SWCNT-CMC. The tiny size of the molecules allows for unrestricted movement and therefore micro-convection, which can somewhat affect heat transmission, which is mitigated by the nanoparticle volume fraction parameter. The heat transmission of both nanofluids is increased, although MWCNT-CMC exhibits better transmission than SWCNT-CMC because MWCNT-CMC is a better heat sink than SWCNT-CMC. As shown in Table 4, increased radiation can increase HT rates. Radiation is well-known as the fastest method for transferring heat, as it emits electromagnetic waves from a body to a receiver. Radiation affects MWCNT-CMC more than SWCNT-CMC. Thus, radiation can be used as a catalyst to enhance heat transmission for MWCNT -CMC.

Table 5. Calculation of Nusselt number $= N_u Re_x^{\frac{-1}{2}}$ for $Pr = 0.8$.

B_ς	Λ	S	ϕ	Nr	Pr	$N_u Re_x^{\frac{-1}{2}}$ MWCNT-CMC	$N_u Re_x^{\frac{-1}{2}}$ SWCNT-CMC
0.1	0.2	0.1	0.1	0.1	0.8	0.0907	0.1209
0.2						0.1735	0.2302
0.3						0.2492	0.3291
	0.1					0.0860	0.1021
	0.2					0.0907	0.1209
	0.3					0.0955	0.1408
		0.1				0.0907	0.1209
		0.2				0.0952	0.1387
		0.3				0.0981	0.1454

0.01			0.0652	0.0979
0.05			0.0780	0.1009
0.1			0.0907	0.1209
	0.1		0.0907	0.1209
	0.2		0.0920	0.1513
	0.3		0.0982	0.1625
		0.8	0.0907	0.1209
		7.8	0.0959	0.1598
		6450	0.0972	0.1853

8. Final Outcomes

In this study, we theoretically investigated the thermal and entropy performance of third-grade nanofluid. The governing equations are converted to ordinary differential equations and numerically resolved using the Galerkin finite element method. All of the findings have been thoroughly examined and debated. As a result of this research, the following conclusions can be drawn:

- ✓ The velocity profile can be increased by adjusting the Deborah number ($\boldsymbol{\beta_2}$, $\boldsymbol{\beta_3}$) and injection parameters, although porous media, volume fraction nanoparticles, velocity slide, and force parameters reduce the speed of the movement.
- ✓ The Deborah number ($\boldsymbol{\beta_1}$), porous media, volume fraction nanoparticle, velocity slip, Biot number, radiation, thermal conductivity, and injection parameter increase the temperature profile, whereas Deborah number ($\boldsymbol{\beta_2}$) and the suction parameter reduce the temperature profile of both nanofluids.
- ✓ Porous media, volume fraction nanoparticles, Biot number, radiation, suction, Reynolds number, and Brinkmann support entropy in the system. However, only velocity slip and injection parameters can reduce flow entropy.
- ✓ The local Nusselt number is determined as a result of the volume fraction nanoparticle, Biot number, and radiation parameter, although it is reduced by the velocity slip parameter.
- ✓ The SWCNT-CMC is a better heat conducting, whereas the MWCNT -CMC is a better heat absorber.

Future applications of the G-FEM include a range of physical and technological difficulties [66–77]. According to [78–87], there have been several recent advancements with respect to the importance of the research domain under consideration.

Author Contributions: Conceptualization, I.U.; Data curation, I.U.; Formal analysis, N.A.A.M.N. and R.W.I.; Funding acquisition, S.M.H. and M.K.; Investigation, W.J.; Methodology, W.J. and S.M.H.; Project administration, M.B.H.; Resources, M.B.H.; Software, F.S.; Supervision, M.K.; Validation, R.W.I.; Visualization, N.A.A.M.N.; Writing—original draft, R.S. and R.W.I.; Writing—review & editing, E.S.M.T.E.D. All authors have read and agreed to the published version of the manuscript.

Funding: This research received no external funding.

Institutional Review Board Statement: Not applicable.

Informed Consent Statement: Not applicable.

Data Availability Statement: All the used data is provided in the manuscript.

Acknowledgments: The authors are grateful to the Deanship of Scientific Research, Islamic University of Madinah, Ministry of Education, KSA, for supporting this research work through a research project grant under Research Group Program/1/804.

Conflicts of Interest: The authors declare no conflict of interest.

References

1. Bergman, T.L.; Lavine, A.S.; Incropera, F.P.; DeWitt, D.P. *Introduction to Heat Transfer*; John Wiley & Sons: Hoboken, NJ, USA, 2011.
2. Serrano, J.; Olmeda, P.; Arnau, F.; Reyes-Belmonte, M.; Lefebvre, A. Importance of heat transfer phenomena in small turbochargers for passenger car applications. *SAE Int. J. Engines* **2013**, *6*, 716–728.
3. Zhang, H.; Zhuang, J. Research, development and industrial application of heat pipe technology in China. *Appl. Therm. Eng.* **2003**, *23*, 1067–1083.
4. Ramesh, K.N.; Sharma, T.K.; Rao, G.A.P. Latest advancements in heat transfer enhancement in the micro-channel heat sinks: A review. *Arch. Comput. Methods Eng.* **2021**, *28*, 3135–3165.
5. Pozhar, L.A. Structure and dynamics of nanofluids: Theory and simulations to calculate viscosity. *Phys. Rev. E* **2000**, *61*, 1432.
6. Rafati, M.; Hamidi, A.A.; Niaser, M.S. Application of nanofluids in computer cooling systems (heat transfer performance of nanofluids). *Appl. Therm. Eng.* **2012**, *45*, 9–14.
7. Polidori, G.; Fohanno, S.; Nguyen, C.T. A note on heat transfer modelling of Newtonian nanofluids in laminar free convection. *Int. J. Therm. Sci.* **2007**, *46*, 739–744.
8. Huminic, G.; Huminic, A. Application of nanofluids in heat exchangers: A review. *Renew. Sustain. Energy Rev.* **2012**, *16*, 5625–5638.
9. Schlichting, H.; Gersten, K. *Boundary-Layer Theory*; Springer Science & Business Media: Berlin/Heidelberg, Germany, 2003.
10. Rivlin, R.S.; Ericksen, J.L. *Stress-Deformation Relations for Isotropic Materials*; Springer: New York, NY, USA, 1997.
11. Hayat, T.; Naz, N.; Asghar, S.; Mesloub, S. Soret-Dufour effects on three-dimensional flow of third grade fluid. *Nucl. Eng. Des.* **2012**, *243*, 1–14.
12. Mustafa, T. Flow and heat simultaneously induced by two stretchable rotating disks. *Phys. Fluids* **2016**, *28*, 043601.
13. Shehzad, S.A.; Hussain, T.; Hayat, T.; Ramzan, M.; Alsaedi, A. Boundary layer flow of third grade nanofluid with Newtonian heating and viscous dissipation. *J. Cent. South Univ.* **2015**, *22*, 360−367.
14. Sajid, M.; Mahmood, R.; Hayat, T. Finite element solution for flow of a third grade fluid past a horizontal porous plate with partial slip. *Comput. Math. Appl.* **2008**, *56*, 1236–1244.
15. Rashidi, M.M.; Shahmohamadi, H.; Dinarvand, S. Analytic approximate solutions for unsteady two-dimensional and axisymmetric squeezing flows between parallel plates. *Math. Probl. Eng.* **2008**, *2008*, 1–13.
16. Shehzad, S.A.; Abbasi, F.M.; Hayat, T.; Ahmad, B. Cattaneo-Christov heat flux model for third-grade fluid flow towards exponentially stretching sheet. *Appl. Math. Mech.* **2016**, *37*, 761–768.
17. Hussnain, M.; Mehmood, A.; Ali, A. Three-dimensional channel flow of second grade fluid in rotating frame. *Appl. Math. Mech.* **2012**, *3*, 289–302.
18. Baris, S. Steady three-dimensional flow of a second grade fluid towards a stagnation point at a moving flat plate. *Turk. J. Eng. Environ. Sci.* **2003**, *27*, 21–29.
19. Shoaib, M.; Siddiqui, A.M.; Rana, M.A.; Imran, A. Three-dimensional flow of a second grade fluid along an infinite horizontal plane wall with periodic suction. *Am. Acad. Sci. Res. J. Eng. Technol. Sci.* **2016**, *18*, 153–170.
20. Ramzan, M.; Bilal, M.; Farooq, U.; Chung, J.D. Mixed convective radiative flow of second grade nanofluid with convective boundary conditions: An optimal solution. *Results Phys.* **2016**, *6*, 796–804.
21. Mustafa, M.; Nawaz, M.; Hayat, T.; Alsaedi, A. MHD boundary layer flow of second grade nanofluid over a stretching sheet with convective boundary conditions. *J. Aerosp. Eng.* **2014**, 27, 1943–5525.
22. Alzahrani, E.O.; Shah, Z.; Dawar, A.; Malebary, S.J. Hydromagnetic mixed convective third grade nanomaterial containing gyrotactic microorganisms toward a horizontal stretched surface. *Alex. Eng. J.* **2019**, *58*, 1421–1429.
23. Fosdick, R.L.; Rajagopal, K.R. Thermodynamics and stability of fluids of third grade. *Proc. R. Soc. Lond. A* **1980**, *339*, 351–377.
24. Yurusoy, M.; Pakdemirli, M. Approximate analytical solutions for the flow of a third grade fluid in a pipe. *Int. J. Non Linear Mech.* **2002**, *37*, 187–195.
25. Ellahi, R.; Riaz, A. Analytical solutions for MHD flow in a third-grade fluid with variable viscosity. *Math. Comp. Model.* **2010**, *52*, 1783–1793.
26. Adesanya, S.O.; Makind, O.D. Thermodynamic analysis for a third grade fluid through a vertical channel with internal heat generation. *J. Hydrodynam.* **2015**, *27*, 264–272.
27. Hayat, T.; Nazar, H.; Imtiaz, M.; Alsaedi, A.; Ayub, M. Axisymmetric squeezing flow of third grade fluid in presence of convective conditions. *Chin. J. Phys.* **2017**, *55*, 738–754.
28. Akinshilo, A.T.; Sobamowo, G.M. Perturbation solutions for the study of MHD blood as a third grade nanofluid transporting gold nanoparticles through a porous channel. *J. Appl. Comp. Mech.* **2017**, *3*, 103–113.
29. Reddy, G.J.; Hiremath, A.; Kumar, M. Computational modeling of unsteady third grade fluid flow over a vertical cylinder: A study of heat transfer visualization. *Res. Phys.* **2018**, *8*, 671–682.
30. Gaffar, S.A.; Prasad, V.R.; Bég, O.A.; Khan, M.H.H.; Venkatadri, K. Radiative magnetohydrodynamics flow of third-grade viscoelastic fluid past an isothermal inverted cone in the presence of heat generation/absorption. *J. Braz. Soc. Mech. Sci. Eng.* **2018,** *40*, 127.
31. Sajid, M.; Mughees, M.; Ali, N. A theoretical analysis of blade coating for third-grade fluid. *J. Plast. Film. Sheeting* **2019,** *35*, 218-338.

32. Mahanthesh, B.; Joseph, T.V. Dynamics of magneto-nano third-grade fluid with Brownian motion and thermophoresis effects in the pressure type die. *J. Nanofluids* **2019**, *8*, 870–875.
33. Waqas, M.; Khan, M.I.; Hayat, T.; Farooq, S.; Alsaedi, A. Interaction of thermal radiation in hydromagnetic viscoelastic nanomaterial subject to gyrotactic microorganisms. *Appl. Nanosci.* **2019**, *9*, 1193–1204.
34. Shah, Z.; Babazadeh, P.; Kumam, A.; Shafee, P. Thounthong, Magnetohydrodynamic nanofluids under the influence of shape factor and thermal transport in a porous media using CVFEM. *Front. Phys.* **2019**, *7*, 164.
35. Shah, Z.; Kumam, P.; Dawar, A.; Alzahrani, E.O.; Thounthong, P. Study of the couple stress convective micropolar fluid flow in a hall MHD generator system. *Front. Phys.* **2019**, *7*, 171.
36. Al-Kouz, W.; Medebber, M.A.; Elkotb, M.A.; Abderahmane, A.; Aimad, K.; Al-Farhany, K.; Jamshed, W.; Moria, H.; Aldawi, F.; Saleel, C.A.; et al. Galerkin finite element analysis of Darcy-Brinkman-Forchheimer natural convective flow in conical annular enclosure with discrete heat sources. *Energy Rep.* **2021**, *7*, 6172–6181.
37. Hatami, M.; Ghasemi, S.E. Thermophoresis and Brownian diffusion of nanoparticles around a vertical cone in a porous media by Galerkin finite element method (GFEM). *Case Stud. Therm. Eng.* **2021**, *28*, 101627.
38. Al-Kouz, W.; Bendrer, B.A.; Aissa, A.; Almuhtady, A.; Jamshed, W.; Nisar, K.S.; Mourad, A.; Alshehri, N.A.; Zakarya, M. Galerkin finite element analysis of magneto two-phase nanofluid flowing in double wavy enclosure comprehending an adiabatic rotating cylinder. *Sci. Rep.* **2021**, *11*, 16494.
39. Khan, R.M.; Imran, N.; Mehmood, Z.; Sohail, M. A Petrov-Galerkin finite element approach for the unsteady boundary layer upper-convected rotating Maxwell fluid flow and heat transfer analysis. *Waves Random Complex Media* **2022**, 1–18. https://doi.org/10.1080/17455030.2022.2055201.
40. Abbas, S.Z.; Wang, X.; Khan, W.A.; Hobiny, A.; Iqbal, K. Finite element analysis of nanofluid flow and heat transfer in a square cavity with two circular obstacles at different positions in the presence of magnetic field. *J. Energy Storage* **2022**, *51*, 104462.
41. Qureshi, M.A.; Hussain, S.; Sadiq, M.A. Numerical simulations of MHD mixed convection of hybrid nanofluid flow in a horizontal channel with cavity: Impact on heat transfer and hydrodynamics forces. *Case Stud. Therm. Eng.* **2021**, *27*, 101321.
42. Asmadi, M.S. Kasmani, R.M.; Siri, Z.; Saleh, H. Galerkin finite element analysis of buoyancy-driven heat transfer of water-based Cu-Al2O3 hybrid nanofluid inside a u-shaped enclosure with localized heat. *J. Enhanc. Heat Transf.* **2022**, *29*, 1–26.
43. Ibrahim, W.; Gadisa, G. Finite element solution of nonlinear convective flow of Oldroyd-B fluid with Cattaneo-Christov heat flux model over nonlinear stretching sheet with heat generation or absorption. *Propuls. Power Res.* **2020**, *9*, 304–315.
44. Mourad, A.; Aissa, A.; Mebarek-Oudina, F.; Jamshed, W.; Ahmed, W.; Ali, H.M.; Rashad, A.M. Galerkin finite element analysis of thermal aspects of Fe_3O_4-MWCNT/water hybrid nanofluid filled in wavy enclosure with uniform magnetic field effect. *Int. Commun. Heat Mass Transf.* **2021**, *126*, 105461.
45. Abbas, I.A. Three-phase lag model on thermoelastic interaction in an unbounded fiber-reinforced anisotropic medium with a cylindrical cavity. *J. Comput. Theor. Nanosci.* **2014**, *11*, 987–992.
46. Abbas, I.A. Generalized magneto-thermoelasticity in a nonhomogeneous isotropic hollow cylinder using the finite element method. *Arch. Appl. Mech.* **2009**, *79*, 41–50.
47. Espinoza, C.; Ramos-Moore, E.; Celentano, D. Effect of microstructure on thermoelastic stresses in Al_2O_3/Ti (C, N, O)/Ti (C, N) coating systems studied by Finite Element Method simulations. *Mater. Lett.* **2021**, *295*, 129777.
48. Bhattacharyya, A.; Sharma, R.; Hussain, S.M.; Chamkha, A.J.; Mamatha, E. A numerical and statistical approach to capture the flow characteristics of Maxwell hybrid nanofluid containing copper and graphene nanoparticles, *Chin. J. Phys.* **2022**, *77*, 1278-1290.
49. Hussain, S.M. Dynamics of ethylene glycol-based graphene and molybdenum disulfide hybrid nanofluid over a stretchable surface with slip conditions. *Sci. Rep.* **2022**, *12*, 1751.
50. Aiboud, S.; Saouli, S. Entropy analysis for viscoelastic magnetohydrodynamic flow over a stretching surface. *Int. J. Nonlinear Mech.* **2010**, *45*, 482–489.
51. Makinde, O.D. Second law analysis for variable viscosity hydromagnetic boundary layer flow with thermal radiation and Newtonian heating. *Entropy* **2011**, *13*, 1446–1464.
52. Loganathan, K.; Mohana, K.; Mohanraj, M.; Sakthivel, P.; Rajan, S. Impact of third grade nanofluid flow across a convective surface in the presence of inclined Lorentz force: An approach to entropy optimization. *J. Therm. Anal. Calorim.* **2021**, *144*, 1935–1947.
53. Loganathan, K.; Rajan, S. An entropy approach of Williamson nanofluid flow with Joule heating and zero nanoparticle mass flux. *J. Therm. Anal. Calorim.* **2020**, *141*, 2599–2612.
54. Rossi, T.F.; McNeil, S.; Hendrickson, C. Entropy model for consistent impact-fee assessment. *J. Urban Plan. Dev.* **1989**, *115*, 51–63.
55. Herniter, J.D. An entropy model of brand purchase behavior. *J. Mark. Res.* **1973**, *10*, 361–375.
56. Torres-Mendieta, R.; Mondragón, R.; Puerto-Belda, V.; Mendoza-Yero, O.; Lancis, J.; Juliá, J.E.; Mínguez-Vega, G. Characterization of tin/ethylene glycol solar nanofluids synthesized by femtosecond laser radiation. *Chem. Phys. Chem.* **2017**, *18*, 1055–1060.
57. Khan, I.J.; Khan, S.A.; Hayat, T.; Alsaedi, A. Entropy Optimization in Magnetohydrodynamic Flow of Third-Grade Nanofluid with Viscous Dissipation and Chemical Reaction. *Iran. J. Sci. Technol. Trans. A Sci.* **2019**, *43*, 2679–2689.
58. Qureshi, M.A. Thermal Capability and Entropy Optimization for Prandtl-Eyring Hybrid Nanofluid Flow in Solar Aircraft Implementation. *Alex. Eng. J.* **2022**, *61*, 5295–5307.

59. Rehman, A.U.; Mehmood, R.; Nadeem, S.; Akbar, N.S.; Motsa, S.S. Effects of single and multi-walled carbon nano tubes on water and engine oil based rotating fluids with internal heating. *Adv. Powder Technol.* **2017**, *28*, 1991–2002.
60. Rehman, S.; Shah, R.A.; Idrees, M.; Khan, A. Mixed convection MHD fows of Ag, Cu, TiO2 and Al2O3 nanofuids over in unsteady stretching sheet in the presence of heat generation along with radiation\absorption effects. *Appl. Nanosci.* **2021**. https://doi.org/10.1007/s13204-020-01666-7.
61. Brewster, M.Q. Thermal radiative transfer and features. John Wiley and Sons: Hoboken, NJ, USA, 1992.
62. Bouslimi, J.; Alkathiri, A.A.; Alharbi, A.N.; Jamshed, W.; Eid, M.R.; Bouazizi, M.L. Dynamics of convective slippery constraints on hybrid radiative Sutterby nanofluid flow by Galerkin finite element simulation. *Nanotechnol. Rev.* **2022**, *11*, 1219–1236.
63. Hussain, S.M.; Jamshed, W.; Safdar, R.; Shahzad, F.; Nasir, N.A.A.M.; Ullah, I. Chemical reaction and thermal characteristics of Maxwell nanofluid flow-through solar collector as a potential solar energy cooling application: A modified Buongiorno's model. *Energy Environ.* **2021**, 1–24. https://doi.org/10.1177/0958305X221088113.
64. Jamshed, W.; Eid, M.R.; Nisar, K.S.; Nasir, N.A.A.M.; Edacherian, A.; Saleel, C.A.; Vijayakumar, V. A numerical frame work of magnetically driven Powell-Eyring nanofluid using single phase model. *Sci. Rep.* **2021**, *11*, 16500.
65. Qureshi, M.A. A Case Study of MHD Driven Prandtl-Eyring Hybrid Nanofluid Flow Over a Stretching Sheet with Thermal Jump Conditions. *Case Stud. Therm. Eng.* **2021**, *28*, 101581.
66. Jamshed, W.; Aziz, A. Entropy Analysis of TiO2-Cu/EG Casson Hybrid Nanofluid via Cattaneo-Christov Heat Flux Model. *Appl. Nanosci.* **2018**, *8*, 1–14.
67. Jamshed, W.; Nisar, K.S. Computational single phase comparative study of Williamson nanofluid in parabolic trough solar collector via Keller box method. *Int. J. Energy Res.* **2021**, *45*, 10696–10718.
68. Jamshed, W.; Devi, S.U.; Nisar, K.S. Single phase-based study of Ag-Cu/EO Williamson hybrid nanofluid flow over a stretching surface with shape factor. *Phys. Scr.* **2021**, *96*, 065202.
69. Jamshed, W.; Nisar, K.S.; Ibrahim, R.W.; Shahzad, F.; Eid, M.R. Thermal expansion optimization in solar aircraft using tangent hyperbolic hybrid nanofluid: A solar thermal application. *J. Mater. Res. Technol.* **2021**, *14*, 985–1006.
70. Jamshed, W.; Nisar, K.S.; Ibrahim, R.W.; Mukhtar, T.; Vijayakumar, V.; Ahmad, F. Computational frame work of Cattaneo-Christov heat flux effects on Engine Oil based Williamson hybrid nanofluids: A thermal case study. *Case Stud. Therm. Eng.* **2021**, *26*, 101179.
71. Jamshed, W.; Mishra, S.R.; Pattnaik, P.K.; Nisar, K.S.; Devi, S.S.U.; Prakash, M.; Shahzad, F.; Hussain, M.; Vijayakumar, V. Features of entropy optimization on viscous second grade nanofluid streamed with thermal radiation: A Tiwari and Das model. *Case Stud. Therm. Eng.* **2021**, *27*, 101291.
72. Jamshed, W.; Nasir, N.A.A.M.; Isa, S.S.P.M.; Safdar, R.; Shahzad, F.; Nisar, K.S.; Eid, M.R.; Abdel-Aty, A.H.; Yahia, I.S. Thermal growth in solar water pump using Prandtl–Eyring hybrid nanofluid: A solar energy application. *Sci. Rep.* **2021**, *11*, 18704.
73. Jamshed, W.; Shahzad, F.; Safdar, R.; Sajid, T.; Eid, M.R.; Nisar, K.S. Implementing renewable solar energy in presence of Maxwell nanofluid in parabolic trough solar collector: A computational study. *Waves Random Complex Media* **2021**. https://doi.org/10.1080/17455030.2021.1989518.
74. Jamshed, W. Finite element method in thermal characterization and streamline flow analysis of electromagnetic silver-magnesium oxide nanofluid inside grooved enclosure. *Int. Commun. Heat Mass Transf.* **2021**, *130*, 105795.
75. Jamshed, W.; Sirin, C.; Selimefendigil, F.; Shamshuddin, M.D.; Altowairqi, Y.; Eid, M.R. Thermal Characterization of Coolant Maxwell Type Nanofluid Flowing in Parabolic Trough Solar Collector (PTSC) Used Inside Solar Powered Ship Application. *Coatings* **2021**, *11*, 1552.
76. Hussain, S.M. Irreversibility Analysis of Time Dependent Magnetically Driven Flow of Sutterby Hybrid Nanofluid: A Thermal Mathematical Model. *Waves Random Complex Media* **2022**. https://doi.org/10.1080/17455030.2022.2089369.
77. Hussain, S.M.; Goud, B.S.; Madheshwaran, P.; Jamshed, W.; Pasha, A.A.; Safdar, R.; Arshad, M.; Ibrahim, R.W.; Ahmad, M.K. Effectiveness of Nonuniform Heat Generation (Sink) and Thermal Characterization of a Carreau Fluid Flowing across a Nonlinear Elongating Cylinder: A Numerical Study. *ACS Omega* **2022**, *7*, 25309–25320.
78. Shahzad, F.; Jamshed, W.; Pasha, A.A.; Safdar, R.; Alam, M.M.; Arshad, M.; Hussain, S.M.; Krawczuk, M. Thermal cooling process by nanofluid flowing near Stagnating point of expanding surface under induced magnetism Force: A computational case study, *Case Stud. Therm. Eng.* **2022**, *36*, 102190.
79. Hussain, S.M.; Jamshed, W.; Pasha, A.A.; Adil, M.; Akram, M. Galerkin finite element solution for electromagnetic radiative impact on viscid Williamson two-phase nanofluid flow via extendable surface. *Int. Commun. Heat Mass Transf.* **2022**, *137*, 106243.
80. Shahzad, F.; Jamshed, W.; Safdar, R.; Hussain, S.M.; Nasir, N.A.A.M.; Dhange, M.; Nisar, K.S.; Eid, M.R.; Sohail, M.; Alsehli, M.; Elfasakhany, A. Thermal Analysis Characterization of Solar Powered Ship Using Oldroyd Hybrid Nanofluids in Parabolic Trough Solar Collector: An Optimal Thermal Application. *Nanotechnol. Rev.* **2022**, *11*, 2015–2037.
81. Jamshed, W.; Eid, M.R.; Safdar, R.; Pasha, A.A.; Isa, S.S.P.M.; Adil, M.; Rehman, Z.; Weera, W. Solar energy optimization in solar-HVAC using Sutterby hybrid nanofluid with Smoluchowski temperature conditions: A solar thermal application. *Sci. Rep.* **2022**, *12*, 11484.
82. Akgül, E.K.; Akgül, A.; Jamshed, W.; Rehman, Z.; Nisar, K.S.; Alqahtani, M.S.; Abbas, M. Analysis of respiratory mechanics models with different kernels. *Open Phys.* **2022**, *20*, 609–615.
83. Jamshed, W.; Safdar, R.; Rehman, Z.; Lashin, M.M.A.; Ehab, M.; Moussa, M.; Rehman, A. Computational technique of thermal comparative examination of Cu and Au nanoparticles suspended in sodium alginate as Sutterby nanofluid via extending PTSC surface. *J. Appl. Biomater. Funct. Mater.* **2022**, 1–20. https://doi.org/10.1177/22808000221104004.

84. Dhange, M.; Sankad, G.; Safdar, R.; Jamshed, W.; Eid, M.R.; Bhujakkanavar, U.; Gouadria, S.; Chouikh, R. A mathematical model of blood flow in a stenosed artery with post-stenotic dilatation and a forced field. *PLoS ONE* **2022**, *17*, e0266727.
85. Akram, M.; Jamshed, W.; Goud, B.S.; Pasha, A.A.; Sajid, T.; Rahman, M.M.; Arshad, M.; Weera, W. Irregular heat source impact on Carreau nanofluid flowing via exponential expanding cylinder: A thermal case study. *Case Stud. Therm. Eng.* **2022**, *36*, 102190.
86. Shahzad, F.; Jamshed, W.; Ahmad, A.; Safdar, R.; Alam, M.M.; Ullah, I. Efficiency evaluation of solar water-pump using nanofluids in parabolic trough solar collector: 2nd order convergent approach. *Waves Random Complex Media* **2022**. https://doi.org/10.1080/17455030.2022.2083265.
87. Hussain, S.M. Dynamics of radiative Williamson hybrid nanofluid with entropy generation: Significance in solar aircraft. *Sci. Rep.* **2022**, *12*, 8916.